Viscous–Plastic Sea Ice Dynamics with the EVP Model: Linearization Issues

Elizabeth C. Hunke

Group T-3 Fluid Dynamics, Theoretical Division, Los Alamos National Laboratory,
Los Alamos, New Mexico 87545
E-mail: eclare@lanl.gov

Behavior of the elastic–viscous–plastic (EVP) model for sea ice dynamics is explored, with particular attention to a necessary numerical linearization of the internal ice stress term in the momentum equation. Improvements to both the mathematical and numerical formulations of the model have moderated the impact of linearizing the stress term; simulations with the original EVP formulation and the improved version are used to explain the consequences of using different numerical approaches. In particular, we discuss the model behavior in two regimes, low ice concentration such as occurs in the marginal ice zone, and very high ice concentration, where the ice is nearly rigid. Most of these results are highly relevant to the viscous–plastic (VP) ice dynamics model on which the EVP model is based. We provide examples of certain pathologies that the VP model and its numerical formulations exhibit at steady state.   © 2001 Academic Press

Key Words: sea ice; visco-plasticity; constitutive equations; numerical simulation methods.

1. INTRODUCTION

Historically, the ice dynamics component has been the largest impediment to efficient sea ice simulation in coupled ice–ocean numerical models. The viscous–plastic (VP) model for sea ice dynamics [8] has a long history of successful applications in a variety of polar studies. It has been thoroughly validated and demonstrated to be quite useful both in "stand-alone" studies of sea ice and in coupled climate simulations. However, because of large viscosities in regions of nearly rigid ice, the VP model requires implicit, iterative numerical methods, which are time consuming and adapt poorly to parallel computation. To remedy this, we have modified the model by incorporating an elastic closure, which leads to a fully explicit numerical scheme [12].

Since the introduction of the elastic–viscous–plastic (EVP) model there has been renewed interest in the physical details of the VP model that it was intended to emulate, particularly the internal stress state of the ice. Our elastic modification appears in the equation for the ice internal stress, and thus the ice stress lies at the root of differences which appear in EVP and VP simulations of ice velocity. In particular, if proper care is not taken with the VP model, numerical linearization of the stress term in the momentum equation can cause undesirable phenomena such as slow time response to changes in external forcing, unconverged stress states, and anomalously thick boundary layers. The EVP model formulation rectifies some of these problems naturally, but because it is originally based on the VP model, it exhibits some of the same behavior.

For example, linearization of the internal stress term is responsible for a problem that both the VP numerical model and the original EVP formulation exhibited: principal stress states were widely scattered outside the elliptical yield curve. The constitutive law, which is highly nonlinear, must be iterated for the stresses, strain rates, and viscosities defined in the problem to all converge. Several changes have been made to the EVP numerical model since it was originally developed, primarily to address this issue.

A related issue is that the linearization can sometimes destroy the elliptical relationship between the principal stresses, even when the solution is fully converged. We present an example of this behavior in Appendix A.

This paper highlights the role of numerical linearization in numerical simulations. In Section 3 we review the results of a high-resolution EVP–VP comparison [13], in which time response differences became apparent. A better understanding of the model behavior as a result of this comparison led naturally to the improvements in the EVP model presented in Section 4. These improvements ensure that the ice stress state converges to the analytical yield curve which defines the model. Finally, in Sections 5 and 6 we explore the behavior of the EVP model in the two extreme regimes, respectively, low ice concentration, where the ice strength is low and model regularization is unnecessary, and very high ice concentration, where the elastic regularization is most important.

2. MODEL DESCRIPTION

The force balance per unit area in the ice pack is given by a two-dimensional momentum equation,

$$m\frac{\partial u_i}{\partial t} = \frac{\partial \sigma_{ij}}{\partial x_j} + \tau_i, \tag{1}$$

where the stress τ_i depends nonlinearly on the ice velocity, u_i, and represents external surface forcing on the ice due to wind and ocean stresses, sea surface slope, and Coriolis effects. (Table I contains a list of symbols with their definitions and units. For brevity we use the suffix notation in this section, with the usual convention that terms containing a repeated suffix are summed over all possible values of the suffix [2].)

The internal stress of the ice is represented by the tensor σ_{ij}. The visco-plastic rheology proposed by Hibler [8] is given by a constitutive law that relates σ_{ij} and the rates of strain $\dot{\epsilon}_{ij}$ through an internal ice pressure P and nonlinear bulk and shear viscosities, ζ and η,

<div align="center">

TABLE I

Symbols and Units for Variables and Parameters

</div>

Symbol	Definition	Units
c	Fractional area covered by ice, $0 \le c \le 1$	
c_w	Ocean drag coefficient	0.0055
Δ	A function of the strain rates	s^{-1}
Δt	Thermodynamic/advection timestep	3600 s
Δt_e	EVP subcycling timestep	s
$\Delta x, \Delta y$	Grid cell length	1.6×10^4 m
δ_{ij}	Kronecker delta: 1 if $i = j$ and 0 if $i \ne j$	
E	Elastic parameter	N/m
e	Ratio of ellipse major axis length to minor axis length	2
$\dot{\epsilon}_{ij}$	ij-component of rates of strain tensor	s^{-1}
f	Coriolis parameter	1.46×10^{-4} s^{-1}
h	Ice thickness	m
m	Mass per unit area of ice	kg/m^2
P	Internal ice pressure	N/m
ρ_w	Ocean density	1026 kg/m^3
σ_{ij}	ij-component of internal stress tensor	N/m
σ_I, σ_{II}	Principal stresses	N/m
T	Damping timescale	1296 s
t	Independent variable for time	s
τ_i, τ_j (τ_x, τ_y)	Surface stress due to external forcing	N/m^2
τ_{ax}, τ_{ay}	x and y wind stress components	N/m^2
θ	Turning angle	0.436332 radian
U_a, V_a	x and y wind velocity components	m/s
U_w, V_w	x and y ocean current components	m/s
u_i, u_j (u, v)	Ice velocity components	m/s
$\lvert \mathbf{U}_w - \mathbf{u} \rvert$	Speed of ocean current relative to ice	m/s
x_i, x_j (x, y)	Independent variables for space	m
ζ	Bulk viscosity	kg/s
η	Shear viscosity	kg/s

such that the principal components of stress lie on an elliptical yield curve,

$$\frac{1}{2\eta}\sigma_{ij} + \frac{\eta - \zeta}{4\eta\zeta}\sigma_{kk}\delta_{ij} + \frac{P}{4\zeta}\delta_{ij} = \dot{\epsilon}_{ij}, \tag{2}$$

where

$$\dot{\epsilon}_{ij} = \frac{1}{2}\left(\frac{\partial u_i}{\partial x_j} + \frac{\partial u_j}{\partial x_i}\right),$$

and P is related to the ice thickness h and fractional ice coverage c as in [8]:

$$P = (2.75 \times 10^4 \text{ N/m}^2)che^{-20(1-c)}. \tag{3}$$

Here P represents the ice strength, increasing exponentially as $c \to 1$. The viscosities are defined in terms of the strain rates,

$$\zeta = \frac{P}{2\Delta}, \tag{4}$$

$$\eta = \frac{P}{2\Delta e^2}, \tag{5}$$

$$\Delta = \left[(\dot{\epsilon}_{11}^2 + \dot{\epsilon}_{22}^2)(1 + e^{-2}) + 4e^{-2}\dot{\epsilon}_{12}^2 + 2\dot{\epsilon}_{11}\dot{\epsilon}_{22}(1 - e^{-2})\right]^{1/2}, \tag{6}$$

and become infinite in the limit of zero strain rate. Here, $e = 2$ is the ratio of the major and minor axis lengths of the elliptical yield curve, and the viscosities and pressure are "effective" quantities whose units reflect an integration of the three-dimensional equation of motion through the ice thickness in deriving Eq. (1).

To regularize the singularity present in the viscosities, Hibler set upper and lower bounds for the viscosities that depend on the ice thickness and concentration. To obtain realistic ice deformation, however, these bounds must allow several orders of magnitude variation in the viscosities. The viscous–plastic timescale in regions of nearly rigid ice is on the order of 1 s for 100-km grid lengths, and 0.01 s for 10-km grid lengths. This necessitates the use of implicit methods for timesteps larger than a few seconds, particularly on high-resolution grids.

Hunke and Dukowicz [12] present an alternative regularization, accomplished by introducing an elastic contribution to the strain rate in such a way that the EVP and VP models are identical at steady state,

$$\frac{1}{E}\frac{\partial \sigma_{ij}}{\partial t} + \frac{1}{2\eta}\sigma_{ij} + \frac{\eta - \zeta}{4\eta\zeta}\sigma_{kk}\delta_{ij} + \frac{P}{4\zeta}\delta_{ij} = \dot{\epsilon}_{ij}. \tag{7}$$

We take advantage of the steady-state equivalence of the models by choosing parameters so that the elastic waves nearly damp out during subcycling within each timestep. Depending on how the elastic parameter E is chosen, the timescale is 3 to 5 orders of magnitude larger than the VP timescale. Therefore, this formulation can be discretized explicitly with an acceptably long timestep, a great advantage for implementations on parallel machines and highly resolved grids.

3. TIME RESPONSE

The VP model is highly nonlinear, and numerical schemes must include some sort of iterative process in order to accurately capture the transient behavior of the model. Although some authors have noted the need to subcycle the VP model under changes in the forcing because the rheology is slow to converge to steady state (e.g., [6, 8]), many more authors did not heed that advice and used the model with 1-day time steps and daily varying winds (e.g., [5, 9, 10, 14, 16, 17]). More recently, VP modelers have recognized the convergence error and incorporated "pseudo-timestepping," an iterative procedure, into the numerical method (e.g., [1, 7, 11, 18]).

Even under smoothed wind forcing the VP model response can be markedly inaccurate, as we found in realistic Arctic simulations used to compare early formulations of the EVP and VP models [13]. The simulations were driven by 6-h ECMWF atmospheric data for 1990–1994, averaged every 3 days and linearly interpolated to the 4-h timestep.

Although the EVP and VP ice distributions in that study could not be distinguished based on observational data such as SSM/I, we found that the differing treatments of the ice internal stress term by the two numerical schemes led to noticeable differences in the responsiveness of the modeled ice to changes in the wind forcing. In particular, the VP

model showed a much slower response time to changes in the forcing patterns than did the EVP model. Ice in the central Arctic has been observed to respond quickly to changing wind conditions; Campbell notes that floe ice obtains a steady-state motion within a few hours after a change of wind stress [4]. Drifting buoys also exhibit this behavior, as shown in [13].

The difficulty is strictly numerical and arises from a linearization that must be performed to discretize the equations. The problem is most easily illustrated with one-dimensional (zonal) flow. Assuming $(\tau_x, \tau_y) = (\tau, 0)$, $v = 0$ and no variation in the y direction, the VP model equations become

$$m\frac{\partial u}{\partial t} = \frac{\partial \sigma_{11}}{\partial x} + \tau, \tag{8}$$

$$\sigma_{11} = (\zeta + \eta)\frac{\partial u}{\partial x} - \frac{P}{2}, \tag{9}$$

$$\sigma_{12} = 0, \tag{10}$$

$$\sigma_{22} = (\zeta - \eta)\frac{\partial u}{\partial x} - \frac{P}{2}, \tag{11}$$

$$\zeta = \frac{P}{|\partial u/\partial x|}\left(\frac{1}{2\sqrt{1 + e^{-2}}}\right), \tag{12}$$

$$\eta = \zeta/e^2. \tag{13}$$

The nonlinearity is apparent when (12) is combined with (9) and (11). The internal ice stress must be linearized in the discretization; this is what "linearization" refers to in this paper.

At this point, it is convenient to point out the fundamental behavior described by this rheology. When the ice is diverging, $\partial u/\partial x > 0$ and

$$\sigma_{11} = \frac{P}{2}\left(\sqrt{1 + \frac{1}{e^2}} - 1\right).$$

When the ice is converging, $\partial u/\partial x < 0$ and

$$\sigma_{11} = \frac{P}{2}\left(-\sqrt{1 + \frac{1}{e^2}} - 1\right);$$

that is, the ice possesses a bulk strength P against convergence that is not present for diverging conditions. Sea ice is a highly fractured material that resists compression but pulls apart easily.

There are several approaches to solving the equations. Substituting σ_{11} and discretizing the momentum equation (8) in time, we have the standard VP numerical formulation

$$m\frac{u^{n+1} - u^n}{\Delta t} = \frac{\partial}{\partial x}\left[(\zeta + \eta)^n \frac{\partial u}{\partial x}^{n+1}\right] + \tau^n. \tag{14}$$

The superscript n refers to the time discretization associated with the timestep Δt. The VP model is usually solved implicitly with a fairly long timestep, typically a few hours to 1 day. For such long timesteps, the acceleration term on the left can be neglected, and the transition to steady state is given approximately by the transient iterates of the resulting numerical

scheme. Because these iterates are slaved to the timestepping through the acceleration term, solutions of the standard VP model require several timesteps to reach steady state (for constant τ), resulting in the slow response to forcing changes observed in the VP simulations of [13]. A detailed, one-dimensional analysis of this approach is presented in [12]. A "pseudo-timestepping" process has recently been implemented in VP models, which iterates the equation $O(10)$ times during each timestep [7, 18].

A second approach was taken in the original version of EVP [12], which was used for the EVP–VP comparison. The viscosities were held fixed through the timestep Δt (denoted by the superscript n) while the stress and momentum equations were subcycled with a smaller timestep Δt_e (denoted by the superscript k):

$$m\frac{u^{k+1} - u^k}{\Delta t_e} = \frac{\partial}{\partial x}\left[(\zeta + \eta)^n \frac{\partial u}{\partial x}^{k+1}\right] + \tau^n. \tag{15}$$

The reason for implementing the EVP model in this way was to reproduce the results of the standard VP numerical model as closely as possible. Although the viscosities were held constant, subcycling (15) $O(100)$ times on each timestep allowed the velocity to adjust more quickly to changes in the forcing.

A third approach is to include the viscosities in the subcycling, so that the entire momentum equation is subcycled under changes in the forcing τ:

$$m\frac{u^{k+1} - u^k}{\Delta t_e} = \frac{\partial}{\partial x}\left[(\zeta + \eta)^k \frac{\partial u}{\partial x}^{k+1}\right] + \tau^n. \tag{16}$$

This method provides the most accurate approximation of the nonlinear stress σ_{11} and is the objective of improvements to the EVP model described in the next section.

4. EVP MODEL IMPROVEMENTS

Linearization of the internal stress term causes the computed principal stress states to lie outside the elliptical yield curve, a problem that is exhibited by both the VP numerical model and the original EVP formulation. The main problem was that the viscosities were not updated enough during the timestep in either model. The constitutive law, which is highly nonlinear, must be iterated for the stresses, strain rates, and viscosities to all converge to the yield curve.

To address this issue, the EVP numerical model now updates the viscosities during subcycling as in Eq. (16), so that the entire dynamics component is subcycled within the timestep Δt. Taken alone, this change would require an increased number of operations to compute the viscosities and thus would greatly hinder efficient numerical solution of the equations. However, the new dynamics code is roughly as efficient as the earlier version because of a change in the definition of the elastic parameter E. E is now defined in terms of a damping timescale for elastic waves, T, as

$$E = \frac{\zeta}{T},$$

where T is a tunable parameter, $\Delta t_e < T < \Delta t$. (Here, $\Delta t_e = \Delta t / N$ is the dynamics timestep, and N is the number of subcycles.) Then the stress equation (7) becomes

$$\frac{\partial \sigma_{ij}}{\partial t} + \frac{e^2}{2T}\sigma_{ij} + \frac{1-e^2}{4T}\sigma_{kk}\delta_{ij} + \frac{P}{4T}\delta_{ij} = \frac{P}{2T\Delta}\dot{\epsilon}_{ij}. \tag{17}$$

All of the coefficients on the left-hand side are constant except for the last, and P changes only on the longer timestep Δt. This modification compensates for the decreased efficiency of including the viscosity terms in the subcycling, thereby allowing more accurate stress states to be obtained with the same amount of computational work.

We illustrate the improved stress state in a geometrically simplified test problem. The dynamics equations are solved on an 80×80 grid with $\Delta x = \Delta y = 16$ km, $\Delta t = 1$ h, $T = 1296$ s, and $\Delta t_e = 30$ s. The ice distribution is fixed, with constant 2-m ice thickness and a concentration field c that varies linearly in the x-direction from 0 to 1 and is constant in y. Three small, closely spaced islands are included for investigation of model behavior in the Canadian Arctic archipelago, to be discussed in a future publication, and the domain is enclosed by land. Boundary conditions specify zero ice thickness, concentration, velocity, and stress for all land grid cells.

Imposed ocean stresses are circular and centered in the square domain, as shown in Fig. 1a,

$$U_w = +0.1(2y - L_y)/L_y,$$
$$V_w = -0.1(2x - L_x)/L_x,$$

where $0 \le x \le L_x = 1.28 \times 10^6$ m and $0 \le y \le L_y = 1.28 \times 10^6$ m. The wind field (Fig. 1b) consists of a linear, symmetric 5 m/s contribution and a nonlinear, time-dependent contribution that varies 33% from a divergent velocity field whose average amplitude is

a   b
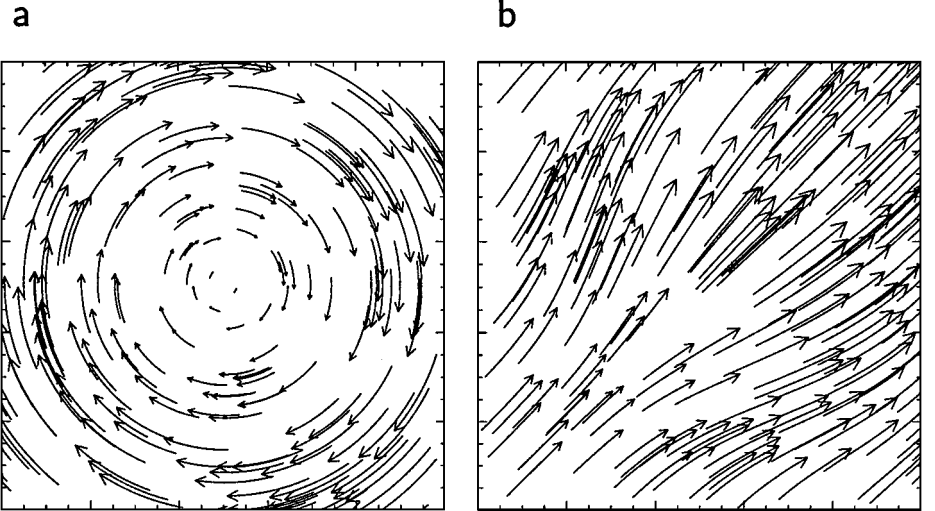
FIG. 1. Streamlines of (a) ocean current and (b) wind fields, proportional in length to the field strength. The current speed ranges from 0 to 0.14 m/s; windspeeds vary between 4 and 10 m/s in this snapshot ($t = 21,600$ s).
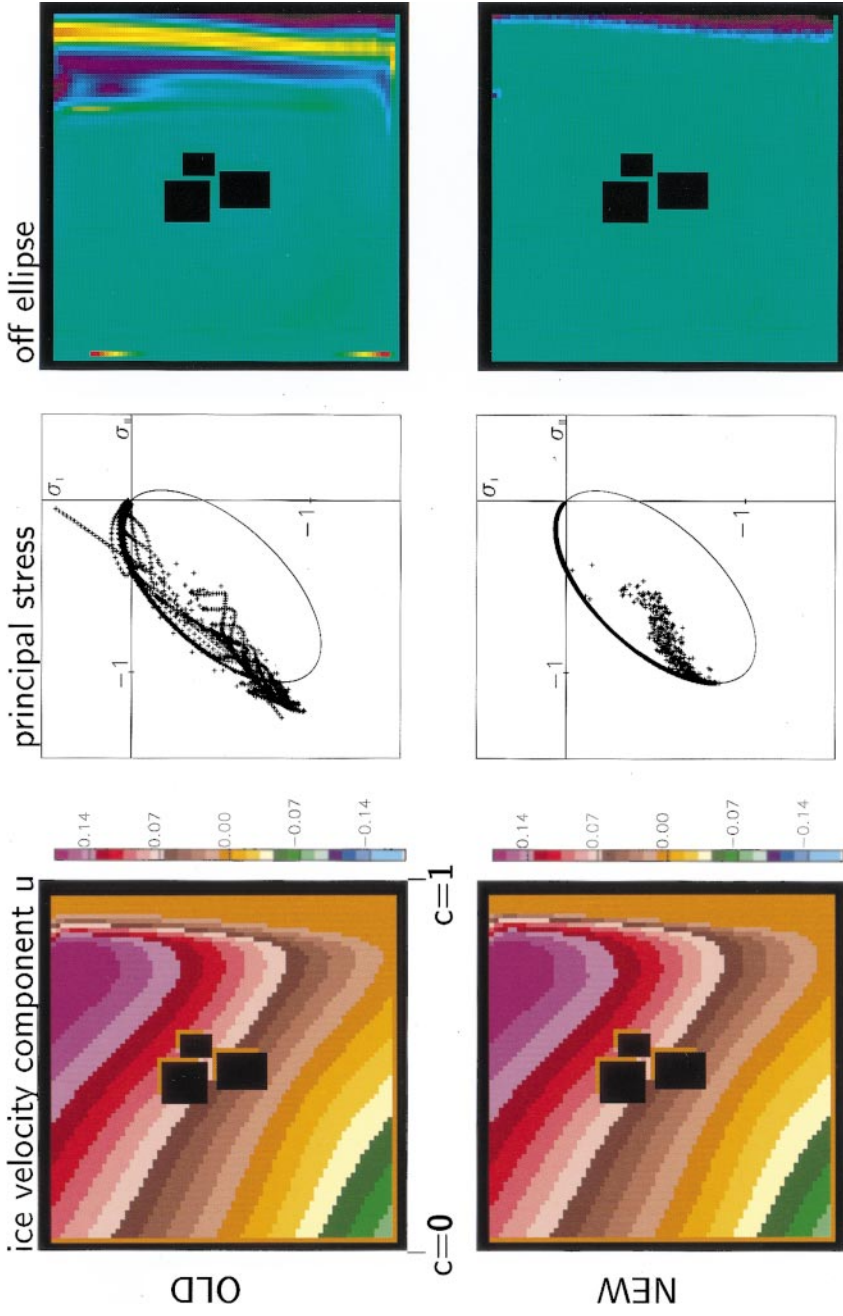
FIG. 2. Ice velocity component u (m/s) and principal stresses for an 80×80 test problem. The top row shows results produced by the original EVP formulation of [12]; the bottom row shows results with the new formulation described in the text. The right column shows which stresses do not lie directly on the ellipse. Blue cells have stresses inside; red and yellow cells have stresses outside. The intensity of the color indicates distance from the ellipse, with red being the farthest away. Green cells have stresses on the ellipse.

3 m/s, with a period $\Theta = 4$ days:

$$U_a = 5 + \left[\sin \left(\frac{2\pi t}{\Theta} \right) - 3 \right] \sin \left(\frac{2\pi x}{L_x} \right) \sin \left(\frac{\pi y}{L_y} \right), \tag{18}$$

$$V_a = 5 + \left[\sin \left(\frac{2\pi t}{\Theta} \right) - 3 \right] \sin \left(\frac{2\pi y}{L_y} \right) \sin \left(\frac{\pi x}{L_x} \right). \tag{19}$$

The wind stress, τ_a, is computed using bulk formulas with stability and quadratic dependence on the wind speed, following [3], with an ice surface roughness length of 5×10^{-4} m.

For these simulations the Coriolis parameter is taken to be constant, and the ocean tilting term is computed from the (geostrophic) currents. The components of the surface stress forcing are then

$$\tau_z = \tau_{ax} + c_w \rho_w |\mathbf{U}_w - \mathbf{u}| [(U_w - u) \cos \theta - (V_w - v) \sin \theta] - mf(V_w - v),$$

$$\tau_y = \tau_{ay} + c_w \rho_w |\mathbf{U}_w - \mathbf{u}| [(V_w - v) \cos \theta + (U_w - u) \sin \theta] + mf(U_w - u),$$

where $\mathbf{U}_w$ is the ocean current and $\theta = 0.436332$ radian ($25°$).

The top row of Fig. 2 shows results produced by the original EVP formulation of [12]; the bottom row shows results with the new formulation. The left column demonstrates that the velocity fields are nearly identical, while the the new formulation's improved stress state is apparent in the middle column: stresses that once lay outside the elliptical yield curve, a physically unrealistic state, are now on or inside the curve.

The normalized principal stress states plotted here and in Section 6, σ_I and σ_{II}, are the eigenvalues of the stress tensor σ_{ij} divided by the pressure P. If there is any ice present in a grid cell, P is nonzero and the ice generally has a nonzero stress state (see Eqs. (9) and (11)). P may be very small, in which case the *non*normalized elliptical yield curve is quite small and lies very close to the origin, corresponding to near-zero stresses and approximate free drift. (If P is identically zero, then there is no ice in the grid cell and the ice stresses are zero by definition.) As long as the viscosity has not reached its maximum limit, the stresses obey the elliptical relationship given by Eqs. (2)–(6); normalizing the stresses with P makes the ellipses a uniform size.

All ice whose viscosity has not reached its maximum limit is assumed to be yielding; its internal stress state lies on the curve and it is said to be in a state of plastic flow, while ice with stresses inside the yield curve is flowing viscously. That is, points whose stresses lie inside the normalized ellipse have reached the maximum viscosity limit, and the rheology is linearly viscous with a constant viscosity. The relationship between the linear viscous principal stresses no longer satisfies (2), and thus the stress states fall inside the elliptical curve.

The right column shows the location of points in the domain which lie inside (blue) or outside (red/yellow) the yield curve; the intensity of the color gives an indication of their distances from the curve. Stresses in green cells lie on the ellipse. Note that ice along the right edge of the domain is in a state of viscous flow for both formulations. In this region the ice concentration is high (greater than 0.9) and the imposed surface stresses are forcing the ice against the right wall. The ice resists such compression with high viscosities that are artificially bounded above, resulting in "creeping" linear viscous flow. The original ("old") formulation limited the viscosity ζ above as in [18] with $\zeta_{\max} = 2.5 \times 10^8 P$ kg/s,

which is equivalent to limiting Δ below (see Eq. (4)) with $\Delta_{min} = 2 \times 10^{-9}$ s^{-1}. In the new formulation, the regularization is achieved through elastic waves instead of creeping flow. However, Δ still appears in the denominator on the right-hand side of Eq. (17), and we set $\Delta_{min} = 10^{-11}$ s^{-1}.

Where ice concentrations are lower than about 0.8 (left four-fifths of the domain), ice strength is low and the ice drifts relatively freely. In this case the ice internal stresses lie on the yield curve, and the constitutive law does not play an important role in the dynamics of the simulated ice pack.

5. VISCOUS EFFECTS IN MARGINAL REGIONS

To ensure against nonlinear instabilities, the original formulation of the VP model included a minimum limit for the viscosity, $\zeta_{min} = 4 \times 10^8$ kg/s [8], although the limiting criterion has been relaxed in subsequent modeling studies [J. Zhang, personal communication]. Analogous to imposing ζ_{max} in regions of high ice concentration, setting such a minimum transforms the rheology from plastic to linear viscous. If the ice velocity varies spatially, then this minimum stress can contribute significantly to the force balance in (1) even though the ice concentration is low enough that the pack should exhibit little or no strength. In a study of floe collisions in the marginal ice zone, where ice concentrations are fairly low, Lu *et al.* [15] note that the computed VP internal ice stress is artificially large compared to the measured data, when the original value of ζ_{min} is used.

The results shown in Fig. 2 were calculated without an imposed minimum viscosity. Figure 3 illustrates the effect of setting $\zeta_{min} = 4 \times 10^8$ kg/s in the original and new versions of the EVP dynamics code. (This limiting is accomplished in the new code by constraining $\Delta < \Delta_{max} = 8 \times 10^8/P$ s^{-1} in Eq. (17).) The minimum viscosity determines the width of the boundary layer by imposing a maximum gradient of the velocity field; that is, ζ_{min} effectively sets maximal strain rates through its dependence on Δ (see Eq. (4)). This limit can be reached easily near land boundaries because $\mathbf{u} = 0$ on land, as is evident in both panels of Fig. 3.

The limit can also be reached in regions where the ice strength P is low and strain rate magnitudes are moderate, as on the left side of the domain in Fig. 3a. Results from the original code reveal a considerable effect where the viscosity is pinned to ζ_{min}. If there is no limit on ζ, as in Fig. 2, then the velocity gradient can be quite large and the boundary layer lies within a grid cell or two of the boundary.

The new formulation of the model does not produce the wide boundary layer at the left side of the domain (Fig. 3b). Because the upper viscosity limit is defined in terms of P and the lower limit is not, there is a range of P for which $\zeta_{max} < \zeta_{min}$. In the original formulation the minimum constraint was applied following the maximum limit on ζ, resulting in the boundary layer seen in Fig. 3a. In the new formulation, the minimum was applied first, followed by the maximum constraint, resulting in very small ζ and a boundary layer less than a grid cell wide.

6. ELASTIC EFFECTS IN RIGID REGIONS

Because of residual elastic waves, ice deformation fields produced by the EVP model can be noisy in regions where the ice is nearly rigid, depending on the choice of parameters
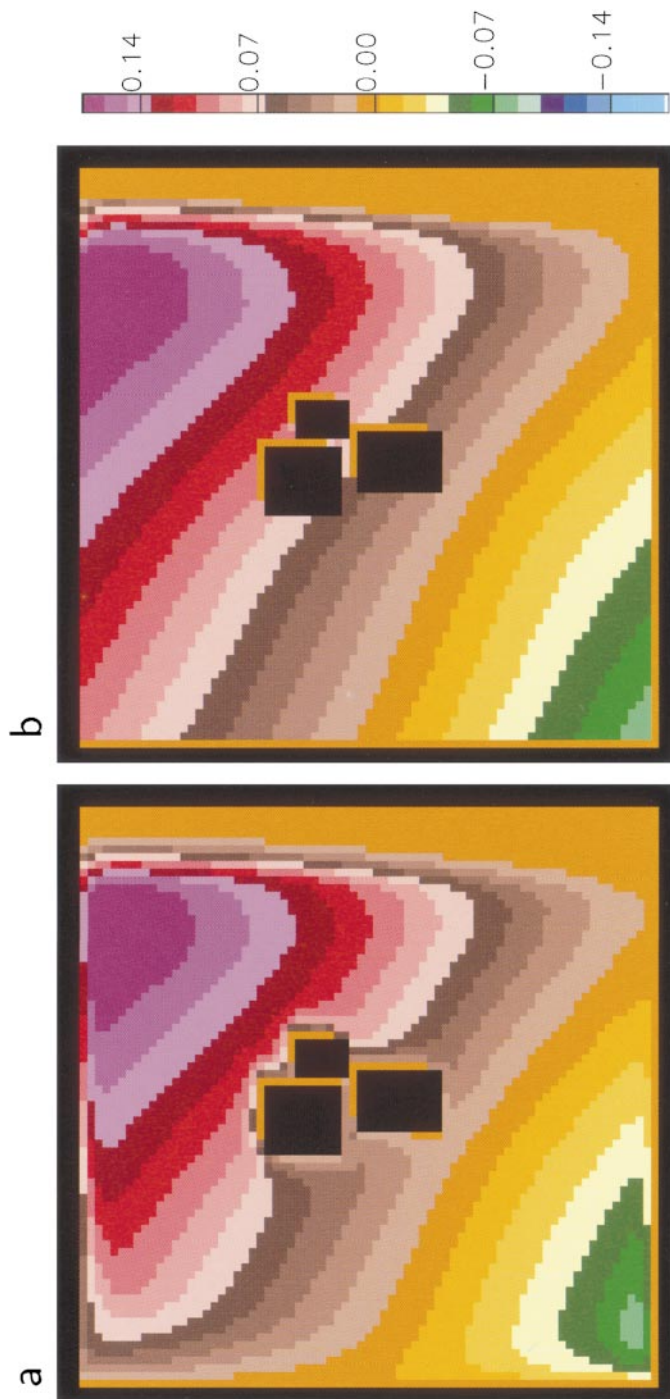
FIG. 3. Ice velocity component u (m/s) produced by the (a) original and (b) new EVP dynamics formulation using $\zeta_{min} = 4 \times 10^8$ kg/s for the test problem described in Section 4. Compare with Fig. 2.

in the model. This problem becomes particularly apparent at high resolution when the prescribed subcycling is insufficient to damp the elastic waves. In regions that should be rigid, waves appear in the deformation field in both space and time, and although the ice velocities are quite small, the differential ice motion from one grid cell to the next can be of considerable magnitude. Ridging schemes for ice thickness distribution models use the ice deformation rates to determine the opening and closing of leads and ice ridging events. Convergence causes the ice in a grid cell to thicken through ridge building. If that grid cell experiences divergence in the next timestep, open water is created in which new ice grows quickly under freezing conditions. This new ice then ridges and the process continues, an effective "pump" forming very thick ice.

The problem originates in the new formulation for the elastic parameter E. In the formulation of [12], E was defined in terms of ice concentration, ice thickness, timestep, and grid size in a manner that guaranteed stability of the solution. The new formulation incorporates the useful concept of a damping timescale for the elastic waves, T, and guarantees stability as long as Δt_e sufficiently resolves T. In other words, the elastic waves will be damped and the solution will converge if Δt_e is chosen small enough to resolve a given T, or if T is chosen long enough to be resolved by a given Δt_e. We will define what we mean by "sufficient resolution" below.

6.1. *Analysis*

Analysis of the stability and damping properties of the model equations aids in understanding the results that follow. To simplify the analysis, we assume one-dimensional zonal flow (that is, $v = 0$ and no variation in the y-direction). At steady state, Eq. (17) can be solved for σ_{11} and σ_{22}. Incorporating the steady-state expression for σ_{22},

$$\sigma_{22} = -\frac{P}{2}\left[\frac{\dot{\epsilon}_{11}}{\Delta}\left(\frac{1}{e^2} - 1\right) + 1\right],$$

into the time-dependent expression for σ_{11} given by Eq. (17), we have

$$\frac{\partial\sigma_{11}}{\partial t} + \frac{1+e^2}{4T}\sigma_{11} = \frac{P}{4T}\left(\frac{1+e^2}{2}\right)\left[\left(\frac{1}{e^2}+1\right)\frac{\dot{\epsilon}_{11}}{\Delta} - 1\right]. \tag{20}$$

To simplify the notation, define

$$A = \frac{1+e^2}{4}, \quad B = \frac{P(1+e^2)^2}{8e^2\Delta}, \tag{21}$$

and consider P and Δ constant for now. Dropping nonhomogeneous terms in Eq. (20) and combining the resulting equation with a homogeneous form of the momentum equation,

$$m\frac{\partial u}{\partial t} = \frac{\partial\sigma_{11}}{\partial x},$$

we obtain a simple wave equation,

$$\frac{\partial^2 u}{\partial t^2} + \frac{A}{T}\frac{\partial u}{\partial t} = \frac{B}{mT}\frac{\partial^2 u}{\partial x^2}. \tag{22}$$

At this point the elastic and viscous–plastic timescales discussed in [12] become evident by relating each of the first two terms with the last and performing a scale analysis:

$$T_e = \sqrt{\frac{mT}{B}} \Delta x, \quad T_v = \frac{mA}{B} \Delta x^2. \tag{23}$$

6.1.1. Damping. Suppose that u takes the form $e^{i(kx-\omega t)}$, and note that only wavenumbers k satisfying $k^2 \Delta x^2 \leq 1$ are meaningful on a grid (now e^x represents the exponential function and $i = \sqrt{-1}$). From Eq. (22) we obtain the dispersion relation

$$\omega^2 + \frac{A}{T} i \omega - \frac{Bk^2}{mT} = 0.$$

Solutions are overdamped when ω is a pure imaginary number, that is, when

$$T < \frac{A^2 m \Delta x^2}{4B}.$$

This result highlights the dependence of damping on the grid scale Δx (for fixed T). Substituting the expressions (21) for A and B, we have

$$T < \frac{e^2 m \Delta x^2 \Delta}{8P}.$$

This relation is easily satisfied in regions where the ice strength given by P is small and rates of strain (Δ) are large; the ice motion is overdamped, and elastic waves do not appear. However, in rigid regions P is large and Δ is small, and the ice motion is underdamped. In this case the decay rate is controlled by the imaginary part of ω, given by $-iA/2T$.

In general, the elastic waves decay faster for smaller values of T, and therefore we want the damping timescale to be as short as possible. If T is too small, however, then Δt_e must be very small and the computational requirement becomes too large for climate studies. Von Neumann stability analysis provides the relationship between T and Δt_e that must be satisfied.

6.1.2. Stability. Now assume that u has the form $a^n e^{ikx}$ and its time dependence satisfies $a^{n+1} = \lambda a^n$. Then the characteristic equation associated with Eq. (22) is

$$\left(1 + \frac{A \Delta t_e}{T}\right) \lambda^2 - \left(2 + \frac{A \Delta t_e}{T} + \frac{Bk^2 \Delta t_e^2}{mT}\right) \lambda + 1 = 0.$$

Solutions are stable whenever $|\lambda| < 1$, that is, for

$$\frac{A \Delta t_e}{T} > \frac{Bk^2 \Delta t_e^2}{2mT} - 2,$$

and using Eqs. (21) and (23), we find the stability region bounded by the hyperbolic function

$$\frac{\Delta t_e}{T_v} = \frac{\left(\frac{\Delta t_e}{T_e}\right)^2}{\frac{1}{2}\left(\frac{\Delta t_e}{T_e}\right)^2 - 2}.$$

(This analysis parallels that in [12], and the stability region is similar to that shown in Fig. 2

of that paper.) Stability is ensured when

$$\frac{\Delta t_e}{T_e} < 2,$$

which translates into the relationship

$$T > \frac{B \Delta t_e^2}{4m \Delta x^2} = \frac{P(1 + e^2)^2 \Delta t_e^2}{32m \Delta x^2 e^2 \Delta}. \tag{24}$$

The objective is to maximize damping while maintaining stability. Again, trouble arises where Δ is small and P, which depends exponentially on the ice concentration, is large: in regions of rigid ice. Two options are to decrease Δt_e or to increase T. We have taken T constant in both space and time (necessary for the efficiency gains discussed in Section 4), and increasing its value degrades the damping characteristics. Decreasing the timestep Δt_e increases the computational time and is not feasible for climate studies. A third option is to limit $B/4m \Delta x^2$ such that (24) is satisfied. This is equivalent to limiting P/Δ, and we use this expression for guidance in the two-dimensional numerical model. In particular, we constrain

$$\frac{P}{\max(\Delta, \Delta_{\min})} < \frac{CT \Delta x \Delta y}{\Delta t_e^2}, \tag{25}$$

where constants and typical mass are incorporated into the tuning parameter C. This constraint effectively allows the waves to damp out more quickly by decreasing the amplitude scaling factor $|\lambda|$.

6.2. Simulation Results

The same test case examined in previous sections is used here to explore the consequences of these choices. Figure 4 shows the ice divergence, velocity, and principal stress components for four different cases. The region of interest is the far right side of the domain, where the ice concentration is close to 1 and the ice should be nearly rigid. The linear component of the applied wind field (see Eqs. (18) and (19)) tends to push the ice toward the upper right corner, shown in the middle column. Because the highly compact ice is confined by the boundary, it resists such compression and exhibits little motion in the corner. There is a sharp shear zone at the left edge of the rigid region, caused by the circular component of the wind stress and the ocean current acting on less compact (and therefore lower strength) ice. The color scale is cropped at $\pm 1.5 \times 10^{-7}$ s^{-1} to show finer detail in the rigid region. For all of these calculations, the damping timescale T is fixed at 1296 s, the forcing changes each hour ($\Delta t = 3600$ s), and the ice dynamics equations are subcycled under the changes in forcing. Table II gives the relevant parameters for each of the cases discussed below.

Row (a) shows the results for $\Delta t_e = 3$ s, which we will refer to as the "converged case." In this case, we increased the subcycling so that $\Delta t_e \ll T$ and Eq. (24) is satisfied. The standard case is shown in row (b), for which $\Delta t_e = 30$ s. The effect of the elastic waves is readily apparent along the right side of the divergence field $\nabla \cdot \mathbf{u}$, although the ice velocity $\mathbf{u}$ is small, similar to the converged case.

The effect of imposing the constraint (25) is shown in row (c) of Fig. 4, using $C = 615$ kg/m^2. The velocities in the rigid region are slightly larger in the damped case than in either the converged or the standard case, but they are still quite small. More importantly for simulations that evolve an ice thickness distribution, the divergence field is much smoother,

TABLE II

Conditions for the Test Cases Shown in Fig. 4

Case	Δt_e	Comments
(a) Converged	3 s	Eq. (25) not enforced
(b) Standard	30 s	Eq. (25) not enforced
(c) Damped	30 s	Eq. (25) enforced
(d) Filtered	30 s	Standard case $+ \mu m \nabla (\nabla \cdot u)$
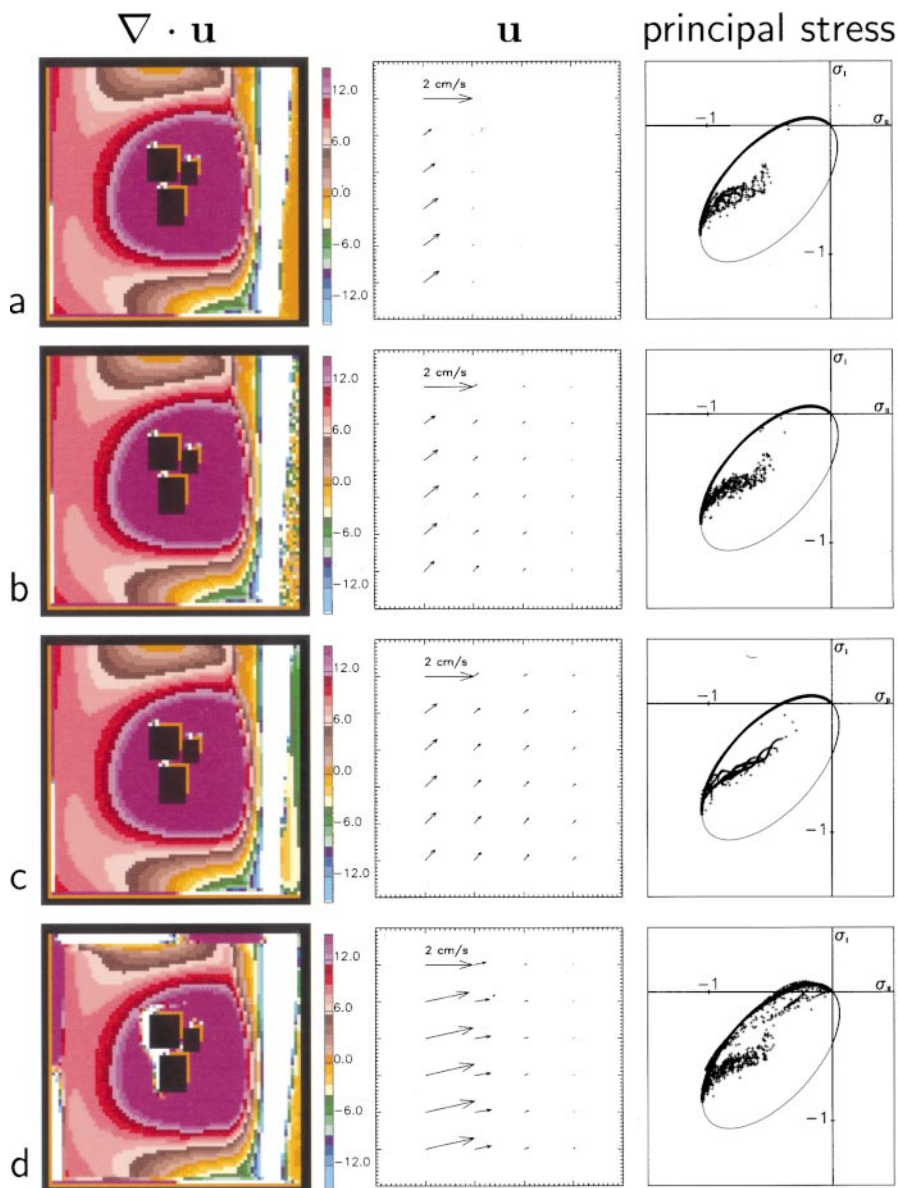
FIG. 4. Divergence (10^{-8} s^{-1}), velocity (m/s) in the top right corner of the domain, and normalized principal stress components for (a) $\Delta t_e = 3$ s, (b) $\Delta t_e = 30$ s (the standard case), (c) $\Delta t_e = 30$ s with damping, and (d) $\Delta t_e = 30$ s with filtering.

although its magnitude is somewhat larger than the converged case (a). Other simulations (not shown) reveal that $\nabla \cdot \mathbf{u}$ in the damped case has the same general pattern and magnitude in rigid regions as the standard case, highly filtered and smoothed.

This similarity is evident in the principal stress states lying in the convergence half of the ellipse (lower left). Recall from Fig. 2 that the stress states lying inside the ellipse are from the rigid region on the far right side of the domain. In this area, the rates of strain become small enough so that the viscosity upper limit (defined by Δ_{min}) comes into play, the stress term in the momentum equation (1) is linearized with constant viscosity, and the normalized stresses fall inside the ellipse. The stress states lying inside the lower left half of the ellipse belong to cells in the far right portion of the domain; the standard case is also convergent there in an average sense, as is the converged case.

It is significant to note that this damping process does not affect the velocity or deformation rates in lower ice concentration regions.

We also explored the possibility of damping the divergence field directly, without significantly changing the velocity field itself. This can be accomplished by adding an explicit damping term to the momentum equation of the form $\mu m \nabla (\nabla \cdot \mathbf{u})$, where μ is a constant damping coefficient. Unfortunately, such an addition causes the subcycling to become unstable. Therefore, rather than include the term during the subcycling process (which is computationally expensive anyhow), we use its mathematical form to create a numerical filter that selectively damps only the divergence field and which is applied following the subcycling. The results are shown in row (d) of Fig. 4, for a run which took three passes through the filter on each timestep Δt. Fewer iterations of the filtering process do not smooth the divergence field sufficiently; more iterations produce a divergence field qualitatively similar in the rigid region to that of the damped case. In lower concentration regions, however, the filtering causes highly erroneous behavior, particularly near sharp edges such as land boundaries. These errors also appear in the velocity field under iterative filtering, as shown in Fig. 4d. Because of this method's computational expense, no attempt was made to selectively apply the filter only in rigid regions.

7. SUMMARY

We developed the EVP model because of its desirable computational characteristics, especially with regard to parallelization issues. In the process we discovered that the EVP model also handles the nonlinear internal ice stress term expediently, overcoming certain difficulties experienced by the VP model. In particular, because of its explicit numerical formulation, the EVP model efficiently updates all rates of strain that determine the ice stress, including the viscosities which traditionally are lagged in the timestepping process. Less error in the nonlinear term allows the EVP model's ice to respond much more quickly to changing surface stress conditions than the VP model's, and the internal ice stress state indicates that the ice is in a state of plastic flow except in highly compact, nearly rigid regions.

In two regimes the original VP model [8] collapses to a linear viscous rheology by limiting the viscosities both above and below, which correspond to high and low ice concentration, respectively. In the original VP and EVP formulations, the lower viscosity limit creates wide boundary layers by limiting the slope of the velocity field. The improved EVP formulation avoids the problem by maintaining consistency of the viscosities and the strain rates through subcycling. In the rigid regime, however, elastic waves introduced in the EVP model do not damp as quickly and can have some effect on ice deformation rates, especially at high resolution. Two methods of damping the waves are presented, termed "filtering" and

"damping" here. Smoothing of the ice divergence using a grad div **u** filter is somewhat effective in highly compact regions, but the iterative process necessary to adequately damp the elastic waves causes large errors in less compact areas. An alternative method involves limiting the quotient P/Δ to maintain effective damping while enforcing a stability criterion in rigid regions. This method is extremely successful at smoothing the ice deformation rates in only the regions needed, but it is not yet known what effect it will have in more realistic simulations that incorporate a sophisticated ice thickness distribution.

Examples presented in the appendixes further illuminate the behavior of the nonlinear internal stress term. While the conditions imposed for these examples may be too restrictive for the VP model's pathological behavior to become apparent in full, two-dimensional simulations, the examples serve to illustrate two important points: (1) one must take care when interpreting numerical results with physical reasoning, as the results may be more a numerical artifact of the discretization method than a physically realistic phenomenon; and (2) under certain forcing conditions, steady-state solutions of the VP model may not be unique, if they exist at all.

In conclusion, this study of the EVP model has illustrated some of the difficulties associated with the numerical solution of viscous–plastic-type sea ice dynamics models. In addition, we have presented a new formulation that improves the modeled stress state, and we have characterized and explained the model's behavior. Because the elastic parameter E has been redefined in the new formulation, the stability criterion enforced by E in the original EVP model must now be incorporated in a different manner, by limiting the quotient P/Δ. This criterion ensures that residual elastic waves in rigid regions are sufficiently damped.

APPENDIX A: LINEARIZATION OF THE ELLIPTICAL YIELD CURVE

Discretization of the visco-plastic stresses destroys the elliptical relationship between the principal stresses, even when the solution is fully converged. To illustrate this, consider the equations for zonal flow (8)–(13) under the following conditions:

$$(\tau_x, \tau_y) = (\tau, 0) \text{ constant,}$$

$$P = \text{constant,}$$

$$\text{boundary conditions:} \quad (u, v) = (0, 0) \quad \text{at } x = 0, L,$$

$$\text{initial conditions:} \quad (u, v) = (0, 0) \quad \text{at } t = 0.$$

We pose the problem at steady state, where the VP and EVP mathematical models are exactly the same, and make no assumptions regarding methods of regularization. The principal stresses can be computed from (9)–(11); they depend on the sign of $\partial u/\partial x$ (divergence or convergence) according to the elliptical yield curve formulation:

$$\frac{\partial u}{\partial x} > 0 \begin{cases} \sigma_{\mathrm{I}} = \left(\frac{\zeta+\eta}{P}\right)\frac{\partial u}{\partial x} - \frac{1}{2}, \\ \sigma_{\mathrm{II}} = \left(\frac{\zeta-\eta}{P}\right)\frac{\partial u}{\partial x} - \frac{1}{2}, \end{cases}$$

$$\frac{\partial u}{\partial x} < 0 \begin{cases} \sigma_{\mathrm{I}} = \left(\frac{\zeta-\eta}{P}\right)\frac{\partial u}{\partial x} - \frac{1}{2}, \\ \sigma_{\mathrm{II}} = \left(\frac{\zeta+\eta}{P}\right)\frac{\partial u}{\partial x} - \frac{1}{2}. \end{cases}$$

Suppose that a small (ε) numerical error occurs during the iteration process, with $\varepsilon \to 0$ as $t \to \infty$:

$$\frac{\partial u}{\partial x}^{n+1} = \left|\frac{\partial u}{\partial x}\right|^n (\pm 1 + \varepsilon).$$

Then the principal stresses become

$$\frac{\partial u}{\partial x} > 0 \begin{cases} \sigma_{\mathrm{I}} = \frac{1}{2}\left(\sqrt{1 + \frac{1}{e^2}}(1 + \varepsilon) - 1\right), \\ \sigma_{\mathrm{II}} = \frac{1}{2}\left(\frac{1 - 1/e^2}{\sqrt{1 + 1/e^2}}(1 + \varepsilon) - 1\right), \end{cases}$$

$$\frac{\partial u}{\partial x} < 0 \begin{cases} \sigma_{\mathrm{I}} = \frac{1}{2}\left(\frac{1 - 1/e^2}{\sqrt{1 + 1/e^2}}(-1 + \varepsilon) - 1\right), \\ \sigma_{\mathrm{II}} = \frac{1}{2}\left(\sqrt{1 + \frac{1}{e^2}}(-1 + \varepsilon) - 1\right). \end{cases}$$

For each case (divergence and convergence) the principal stress formulas may be combined by eliminating ε:

$$\sigma_{\mathrm{I}} = \left(\frac{e^2 + 1}{e^2 - 1}\right)\sigma_{\mathrm{II}} + \left(\frac{1}{e^2 - 1}\right), \quad \frac{\partial u}{\partial x} > 0,$$

$$\sigma_{\mathrm{I}} = \left(\frac{e^2 - 1}{e^2 + 1}\right)\sigma_{\mathrm{II}} - \left(\frac{1}{e^2 + 1}\right), \quad \frac{\partial u}{\partial x} < 0.$$

The relationship between σ_{I} and σ_{II} is linear throughout the iteration, regardless of ε. A nearly converged numerical solution close to steady state is shown in Fig. 5 and illustrates the fact that linearization of the stress fundamentally changes the nature of the rheology near steady state. Neither subcycling the EVP model nor the similar pseudo-timestepping procedure for the VP model alters this steady-state result. Note that these linear features are evident in the 2D simulations shown in Figs. 2 and 4.

APPENDIX B: EXISTENCE AND UNIQUENESS

The VP model exhibits some other peculiar behavior at steady state. Removing all reference to the viscosities (η and ζ) to make the equation's singularities perfectly evident and assuming that there are no variations in y ($\partial_y = 0$), the VP constitutive and momentum equations can be written in the form

$$[(1 + e^2)\sigma_{11} + (1 - e^2)\sigma_{22} + P]\Delta = 2P\partial_x u, \tag{B.1}$$

$$[(1 - e^2)\sigma_{11} + (1 + e^2)\sigma_{22} + P]\Delta = 0, \tag{B.2}$$

$$\sigma_{12}\Delta = \frac{P}{2e^2}\partial_x v, \tag{B.3}$$

$$\partial_x \sigma_{11} = -\tau_x, \tag{B.4}$$

$$\partial_x \sigma_{12} = -\tau_y, \tag{B.5}$$

where

$$\Delta = \frac{1}{e}\left[(\partial_x u)^2(1 + e^2) + (\partial_x v)^2\right]^{1/2} \tag{B.6}$$
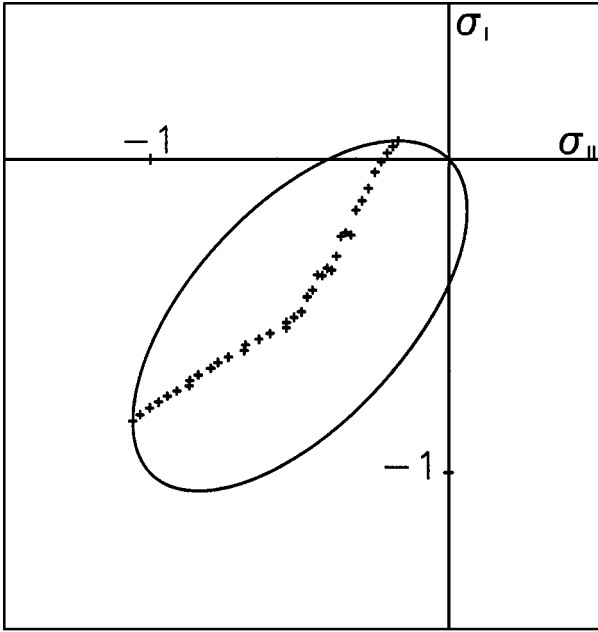
FIG. 5. Principal stresses for the zonal flow problem described in Appendix A, produced by a one-dimensional version of the EVP numerical model similar to that used in [12], but with the improvements described in Section 4. The same linear features are exhibited by stresses in Figs. 2 and 4.

and P is the ice pressure defined in terms of ice concentration and thickness as in Eq. (3). We wish to solve the problem with $(\tau_x, \tau_y) = (0, 0)$ and under the following boundary conditions on the velocity:

$$(u, v) = (0, 0) \quad \text{at } x = 0,$$

$$(u, v) = (0, v_0) \quad \text{at } x = L.$$

That is, there is no surface stress; the motion is driven by the moving right boundary. (Assume $v_0 > 0$.) We will see that solutions exist only for constant, nonzero stresses at the boundaries; we leave these conditions unspecified for now.

The stresses follow from Eqs. (B.4), (B.5), and (B.2),

$$\sigma_{11} = c_1,$$

$$\sigma_{12} = c_2,$$

$$\sigma_{22} = -\frac{P + c_1(1 - e^2)}{1 + e^2},$$

for constants c_1 and c_2 given by the boundary conditions. For now, assume c_1 and c_2 are nonzero. Substituting the stresses into Eqs. (B.1) and (B.3), we have

$$\frac{e^2}{1 + e^2}(2c_1 + P)\Delta = P\partial_x u,$$

$$\Delta = \frac{P}{2e^2 c_2}\partial_x v.$$

Combining these yields $\partial_x u = c_3 \partial_x v$, where

$$c_3 = \frac{2c_1 + P}{2c_2(1 + e^2)}.$$

Integrating and applying the velocity boundary conditions, we find that $u = 0$ and a solution for v exists only if $c_1 = -P/2$. Applying (B.6) to (B.3), we have

$$\Delta = \frac{2}{e}\sqrt{(\partial_x v)^2} = \frac{P}{2e^2 c_2}\partial_x v.$$

By convention, $\Delta > 0$; a solution exists only if $c_2 = P/4e$, but that solution is undetermined. In particular, $v = v_0 x/L$ and $v = v_0 x^2/L^2$ are both solutions to the problem, with $u = 0$, $\sigma_{11} = \sigma_{22} = -P/2$, and $\sigma_{12} = P/4e$.

Note that if σ_{12} is specified to be zero on the boundaries, then $\partial_x v = 0$ by (B.3) and v cannot satisfy its boundary conditions. Similarly, no solution exists if σ_{11} or σ_{22} is zero on the boundaries.

ACKNOWLEDGMENTS

REFERENCES

1. T. E. Arbetter, J. A. Curry, and J. A. Maslanik, Effects of rheology and ice thickness distribution in a dynamic-thermodynamic sea ice model, *J. Phys. Oceanogr.* **29**, 2656 (1999).

2. G. K. Batchelor, *An Introduction to Fluid Dynamics* (Cambridge Univ. Press, Cambridge, UK 1967).

3. F. O. Bryan, B. G. Kauffman, W. G. Large, and P. R. Gent, *The NCAR CSM Flux Coupler*, Technical Note TN-425+STR (National Center for Atmospheric Research, May 1996).

4. W. J. Campbell, The wind-driven circulation of ice and water in a polar ocean, *J. Geophys. Res.* **70**, 3279 (1965).

5. W. L. Chapman, W. J. Welch, K. P. Bowman, J. Sacks, and J. E. Walsh, Arctic sea ice variability: Model sensitivities and a multidecadal simulation, *J. Geophys. Res.* **99**, 919 (1994).

6. G. M. Flato and W. D. Hibler, Modeling pack ice as a cavitating fluid, *J. Phys. Oceanogr.* **22**, 626 (1992).

7. C. A. Geiger, W. D. Hibler, and S. F. Ackley, Large-scale sea ice drift and deformation: Comparison between models and observations in the western Weddell Sea during 1992. *J. Geophys. Res.* **103**, 21893 (1998).

8. W. D. Hibler, A dynamic thermodynamic sea ice model, *J. Phys. Oceanogr.* **9**, 817 (1979).

9. W. D. Hibler and S. F. Ackley, Numerical simulation of the Weddell Sea pack ice, *J. Geophys. Res.* **88**, 2873 (1983).

10. W. D. Hibler and J. E. Walsh, On modeling seasonal and interannual fluctuation of Arctic sea ice. *J. Phys. Oceanogr.* **12**, 1514 (1982).

11. Z. J. Huang and S. B. Savage, Particle-in-cell and finite difference approaches for the study of marginal ice zone problems, *Cold Reg. Sci. Technol.* **28**, 1 (1998).

12. E. C. Hunke and J. K. Dukowicz, An elastic–viscous–plastic model for sea ice dynamics, *J. Phys. Oceanogr.* **27**, 1849 (1997).

13. E. C. Hunke and Y. Zhang, A comparison of sea ice dynamics models at high resolution, *Mon. Weather Rev.* **127**, 396 (1999).

14. C. F. Ip, W. D. Hibler, and G. M. Flato, On the effect of rheology on seasonal sea ice simulations, *Ann. Glaciol.* **15**, 17 (1991).

15. Q. Lu, J. Larsen, and P. Tryde, On the role of ice interaction due to floe collisions in marginal ice zone dynamics, *J. Geophys. Res.* **94**, 14525 (1989).

16. S. H. Riedlinger and R. H. Preller, The development of a coupled ice–ocean model for forecasting ice conditions in the Arctic, *J. Geophys. Res.* **96**, 16955 (1991).

17. J. E. Walsh, W. D. Hibler, and B. Ross, Numerical simulation of Northern Hemisphere sea ice variability, 1951–1980. *J. Geophys. Res.* **90**, 4847 (1985).

18. J. Zhang and W. D. Hibler, On an efficient numerical method for modeling sea ice dynamics, *J. Geophys. Res.* **102**, 8691 (1997).